Improved Microwave Imaging by Wavenumber Domain Multiband Data Fusion

Wang, Jianping; Aubry, Pascal; Yarovoy, Alexander

Improved Microwave Imaging by Wavenumber Domain Multiband Data Fusion

Jianping Wang, Pascal Aubry, and Alexander Yarovoy
Faculty of Electrical Engineering, Mathematics and Computer Science
Delft University of Technology
Delft, the Netherlands, 2628CD
Email: {J.Wang-4, P.J.Aubry, A.Yarovoy}@tudelft.nl

Abstract—A matrix-pencil based wavenumber-domain multiband fusion approach is proposed for improved microwave imaging. The suggested fusion approach is based on the fact from the Born approximation that the wavenumber-domain signal in a given scattering direction can be represented as a sum of the same number of contributions over the whole bandwidth. Utilizing this fact, the wavenumber-domain signal in each radial direction can be modeled as a superposition of damped/undamped exponential functions, where measured multiband data are part of the observations of the whole-band signal. Then the multiband signal fusion is addressed by estimating a unified signal model over the while bandwidth with the matrix pencil approach in the wavenumber domain. By using the estimated signal model, the missing data in the frequency gap can be extrapolated, thus synthesizing an equivalent wideband signal spectrum. After an inverse Fourier transform, the synthesize spectrum leads to a focused image with enhanced resolution. Compared to the existing frequency-domain method, the proposed fusion approach can be used for radar imaging with the signals acquired by either collocated or non-collocated arrays in different frequency bands. The effectiveness and accuracy of the proposed fusion approach are demonstrated through some numerical simulations.

I. INTRODUCTION

Microwave imaging has been broadly used for remote sensing, non-destructive testing (NDT), security check, medical imaging, etc. In these applications, pursuing increasingly high-resolution imaging is always an objective of many researchers. Generally, imaging radar systems exploit wideband signals and antenna arrays to achieve high resolution in both down- and cross-range directions. In terms of down-range resolution, it is inversely proportional to the operational signal bandwidth of the imaging system. So wideband/ultra-wideband (UWB) signals with several GHz or even larger bandwidth are typically required to achieve cm/sub-cm level resolutions, especially for short-range applications. However, to radiate such wideband signals, some challenges/problems are frequently encountered in practical implementations. Firstly, antennas and front-ends with sufficiently wide operational bandwidth are needed. Unfortunately, designing and manufacturing an UWB front-ends including antennas for a particular application is a challenging task, especially for subsurface imaging systems. In practice, the problem is typically circumvented by splitting the desired operational ultrawide bandwidth into several sub-bands over while narrow-band antennas are used to cover the entire desired bandwidth. Moreover, sometimes the availability of continuous wide/UWB spectrum for high-resolution imaging can also be a problem due to constraints of, for example, FCC radio spectrum allocation. In such circumstances, only some separate spectral bands can be used. This problem is encountered by users of commercial UWB radar systems. In addition, sometimes strong interference signals at certain frequency spectrum during the imaging system operation have to been clipped, which leads to non-continuous signal bandwidth. Therefore, in all these situations it becomes essential to coherently process or fuse the subband signals/images acquired in different subbands so as to get high-resolution images.

Multiband signal fusion has been widely discussed to improve the down-range resolution of radar systems [1]–[11]. Generally, the approaches in open literature can be divided into two categories: (1) signal-level fusion, and (2) Data-level fusion. Signal-level fusion methods directly process the multiband signals measured by *monostatic/collocated radars*, which are usually implemented in the frequency domain with model-based estimation methods. The multiband data are modeled with autoregressive (AR) models or autoregressive moving average (ARMA) models over a wide bandwidth according to the scattering behaviors of canonical scatterers. Then the signal models can be estimated with root MUltiple SIgnal Classification (MUSIC) algorithm [1], [3], matrix pencil aproach [4] singular-value decomposition (SVD) [2], sparse Bayesian learning algorithm [5] and support vector machine [6]. In addition, a fusion method that combines all-phase fast Fourier transform (apFFT) and iterative adaptive approach [8] was proposed to fuse the dechirped multiband signals, which is more dedicated to the linear frequency modulated (LFM) signals.

On the other hand, the data-level fusion methods are carried out on the pre-focused data in the frequency-wavenumber/wavenumber domain [9], [11]. More precisely, the fusion operations So it is possible to use these methods to fuse multiband signals acquired with different spatial sampling intervals in the cross-range direction, which is very attractive for many practical cases with multiband fusion imaging. In [9], AR model based multiband coherent signal fusion processing was proposed for inverse synthetic aperture radar imaging (ISAR). The fusion operations are performed in the frequency-wavenumber domain after the cross-range focusing operation, which alleviates the effects of the possible error caused by the bandwidth interpolation/extrapolation in the fusion processing on the cross-range response. Moreover, a Matrix Fourier Transform (MFT) was proposed to integrate multiple separated wavenumber domain data to implement multi-look ISAR images fusion in [11]. However, the frequency gaps between the different subbands are usually neglected, which
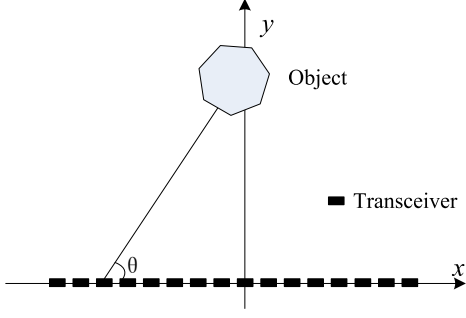
Fig. 1: Geometrical configuration of 2-D imaging with a linear array.

could cause increased sidelobes/artifacts in fused images.

To address the problem of MFT and extrapolate the missing data in the wavenumber domain, we propose a wavenumber-domain (i.e., k-space [12]) multiband signal fusion algorithm with the matrix-pencil approach (named as k-MPA) for enhanced microwave imaging. By modeling the wavenumber-domain signals in each radial direction at different subbands as a superposition of damped/undamped exponential functions, the multiband fusion problem is converted to parameter estimation of the exponential components. Similar to [4], the signal model in each radial direction is estimated by using the matrix-pencil approach for signal extrapolation in the frequency gap between different frequency subbands. Finally, coherently processing the available data and extrapolated one, a resolution-enhanced image can be obtained.

The paper is organized as follows. In Section II, the signal model in k-space is formulated and analyzed for microwave imaging. Following that, the k-space signal fusion is discussed in detail based on the matrix-pencil approach in Section III, which includes both signal incoherence correction and multiband signal fusion. Then, some numerical simulations are performed to demonstrate the effectiveness and accuracy of the proposed approach in Section IV. Finally, some conclusions are drawn in Section VI.

II. k-SPACE SIGNAL FORMULATION

Let us consider the two-dimensional (2-D) imaging configuration, as shown in Fig. 1. A linear antenna array is placed on the x-axis, where $(x_a, 0)$ is used to denote an antenna's position. An illuminated object is located in the near field of the array and its position is represented by (x, y). The associated reflectivity function of the object is given by $f(x, y)$.

After correcting the spectrum weighting of the radiated wavelet and compensating the wave propagation effect (i.e., propagation spreading loss) and the wavefront curvature [13], then the resultant signal spectrum in the 2-D k-space can be represented as

$$S(k_{x_a}, k_y) = \iint_{o(x,y)} f(x, y) \exp[-j(k_{x_a} x + k_y y)] \, dx \, dy \quad (1)$$

In the polar coordinate system, the wavenumbers k_{x_a}, and k_y are expressed as

$$\begin{cases} k_{x_a} = k \cos \theta \\ k_y = k \sin \theta \end{cases} \quad (2)$$

where $k = 4\pi f/c$ is the wavenumber related to the frequency f. θ is the observation angle of an antenna with respect to a scatterer and defined as

$$\theta = \arctan\left(\frac{y}{x - x_a}\right) \quad (3)$$

From (2) and (3), one can see that the point (k_{x_a}, k_y) is located on a circle of the radius k (aka, a slice of Ewald sphere [14]), and for a specific frequency the signal spectra of a point target lie on an arc spanned by the observation angles of the antennas with respect to the target. Meanwhile, from (2), one can see that the signal spectrum of a point target with the increase of the radar signal frequency expands along a radial direction of the polar coordinate system at a given observation angle.

Substituting (2) for k_{x_a} and k_y, (1) can be rewritten as

$$S(k_{x_a}, k_y) = \iint_{o(x,y)} f(x, y) \exp\left[-jk(x \cos \theta + y \sin \theta)\right] dx \, dy$$
$$= S(k, \theta) \quad (4)$$

In a discrete form, the target signal spectrum along a particular radial direction from the origin in the k-space can be represented as

$$S(k, \theta) = \sum_{n=1}^{N} f(x_n, y_n) \exp[-jk \cdot (x_n \cos \theta + y_n \sin \theta)]$$
$$= \sum_{n=1}^{N} f(x_n, y_n) \exp[-jk \cdot d_n(\theta)] \quad (5)$$

where

$$d_n(\theta) = x_n \cos \theta + y_n \sin \theta \quad (6)$$

and $f(x_n, y_n)$ is the reflectivity function of a point-like scatterer at (x_n, y_n), N is the number of point-like scatterers that contribute to the signal spectrum at (k, θ) in the k-space. Note the summation cell $\Delta V = \Delta x \cdot \Delta y$ has been omitted in (5) for simplification. According to (3), the observation angles are just determined by the relative geometry between the antennas and the scatterers, which are independent of the signal frequency. Therefore, assuming the antenna beamwidth at all frequencies is wide enough compared to the imaging area, the number of scatterers N is constant over all the frequencies at a specific aspect angle θ. So the signals at different frequency bands share the same signal model as in (5) where the signal is expressed as a superposition of exponential components. Therefore, the multiband signal fusion can be converted to parameters estimation of exponential damped/undamped sinusoids. By estimating the number of scatterers and the reflectivity function $f(x_n, y_n)$, the signal model in (5) is obtained for a specific aspect θ. Then the signal can be extrapolated based on the estimated signal model.

III. Multiband Signal Fusion

A. Signal Incoherence Compensation

Without loss of generality, two subband signals are considered below. According to (5), the k-space signals in a spherical (polar) coordinate system at the low- and high-frequency subbands can be written as

$$S_1(k_1 + m\Delta k, \theta) = \sum_{n=1}^{N} f(x_n, y_n)$$
$$\times \exp[-j(k_1 + m\Delta k)d_n(\theta)] + n_1(m),$$
$$m = 0, 1, \cdots, M_1 - 1 \quad (7)$$

$$S_2(k_2 + m'\Delta k, \theta) = \sum_{n=1}^{N} f(x_n, y_n) \exp[j(\alpha + \beta m')]$$
$$\times \exp\left[-j(k_2 + m'\Delta k)d_n(\theta)\right] + n_2(m'),$$
$$m' = 0, 1, \cdots, M_2 - 1 \quad (8)$$

where $\Delta k = 4\pi\Delta f/c$ is the wavenumber counterpart of the frequency sampling interval Δf, M_1 and M_2 are the numbers of frequency samples in the two subbands, $k_1 = 4\pi f_1/c$ and $k_2 = 4\pi f_2/c$ are the wavenumbers associated with the starting frequencies f_1 and f_2 of the low- and high-frequency subbands, respectively, and $k_2 > k_1 + M_1\Delta k$. n_1 and n_2 are with zero-mean Gaussian distribution and represent measurement errors and noise. In (8), the first exponential term $\exp[j(\alpha + \beta m')]$ accounts for the phase incoherence between the two subbands which may acquired with different systems. To simplify the notation, $S_1(m)$ and $S_2(m')$ are used to denote $S_1(k_1 + m\Delta k, \theta)$ and $S_2(k_2 + m'\Delta k, \theta)$ below. After some algebraic operations, the signals in both subbands can be rewritten as

$$S_1(m) = \sum_{n=1}^{N} f_n^{(1)} Z_n^m + n_1(m), \ m = 0, 1, \cdots, M_1 - 1 \quad (9)$$

$$S_2(m') = \sum_{n=1}^{N} f_n^{(2)} Z_n'^{m'} + n_2(m'), \ m' = 0, 1, \cdots, M_2 - 1$$
$$(10)$$

where

$$f_n^{(1)} = f(x_n, y_n) \exp\left[-jk_1 \cdot d_n(\theta)\right] \quad (11)$$
$$Z_n = \exp[-j\Delta k \cdot d_n(\theta)] \quad (12)$$
$$f_n^{(2)} = f(x_n, y_n) \exp[j\alpha] \cdot \exp[-jk_2 \cdot d_n(\theta)] \quad (13)$$
$$Z_n' = \exp[-j\Delta k \cdot d_n(\theta) + j\beta] \quad (14)$$

From (11) to (14), it can be seen that the possible phase differences between the two subbands affect both the signal poles and their coefficients in (9) and (10). Specifically, the constant phase difference affects the coefficients while the linear phase difference term rotates signal poles over the unit circle in the complex plane. So, to compensate the phase differences between the two subbands, both signal poles and their coefficients have to be estimated. As the signal models in (9) and (10) basically are the basis all-pole models, their parameters can be estimated with root MUSCI or matrix pencil approach. In this paper, we use the matrix-pencil approach as in [15]. Then the phase differences between different subbands can be corrected.
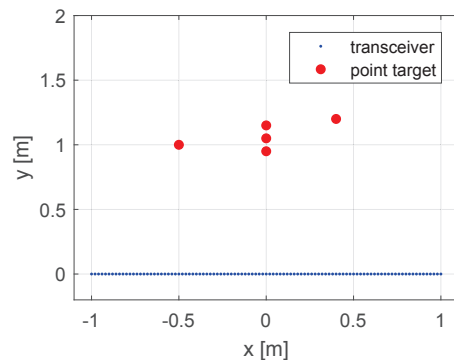

Fig. 2: The geometrical configuration of point-targets simulation.

B. Subband Signal Fusion

After incoherence correction, the k-space coherent multiband signals, i.e., S_1 and S_2', are obtained. For the convenience of notation, S_2' will be replaced by S_2 in the following. The common signal model of the S_1 and S_2 can be expressed as

$$\tilde{S}(k_1 + m\Delta k, \theta) = \sum_{n=1}^{N} \tilde{f}_n \tilde{Z}_n^m + b(m) \quad (15)$$

where $\{\tilde{f}_n\}_{n=1}^N$ and $\{\tilde{Z}_n\}_{n=1}^N$ are the coefficients and the signal poles, respectively. b is the Gaussian noise. The signal poles and their coefficients in (15) can be estimated with the MPA based on the S_1 and S_2 again. After getting the estimations of the signal poles $\{\tilde{Z}_n\}_{n=1}^N$ and their coefficients $\{\tilde{f}_n\}_{n=1}^N$, the full-band signal model in (15) is obtained. Then the full band signals $\tilde{S}(m)$, $m = 0, 1, \cdots, M - 1$, can be estimated, where M is the number of the samples in the full band with sampling intervals of Δk. To refine the estimation of the full band signals, the similar iterative scheme as in [4] is applied.

IV. Numerical Simulations

A. Point Targets

A numerical simulation was performed for point targets with two-band signals. The simulation configuration is illustrated in Fig. 2. Assume a linear antenna array was placed on the x-axis with its center at the origin and the y-axis pointing towards the illuminated scene. The antenna array was 2 m in length and operated in two separate bandwidths, namely, 2–4.5 GHz and 6–8 GHz. Five point targets (i.e., small spheres of the radius 1 cm) were placed at the positions $(-0.5, 1)$m, $(0, 0.95)$m, $(0, 1.05)$m, $(0, 1.15)$ and $(0.4, 1.2)$m, respectively. The Hertz dipole was used as the radiator in the antenna array, and the intervals between antenna elements were 1 cm at both bandwidths. The electromagnetic (EM) data at the two bandwidths were synthesized by the Commercial EM software FEKO with the Method of Moments in the frequency domain with frequency steps of 20 MHz.

Focusing the EM data at the two frequency subbands with the range migration algorithm, the images of the illuminated scene were reconstructed, as shown in Fig. 3. The two focused
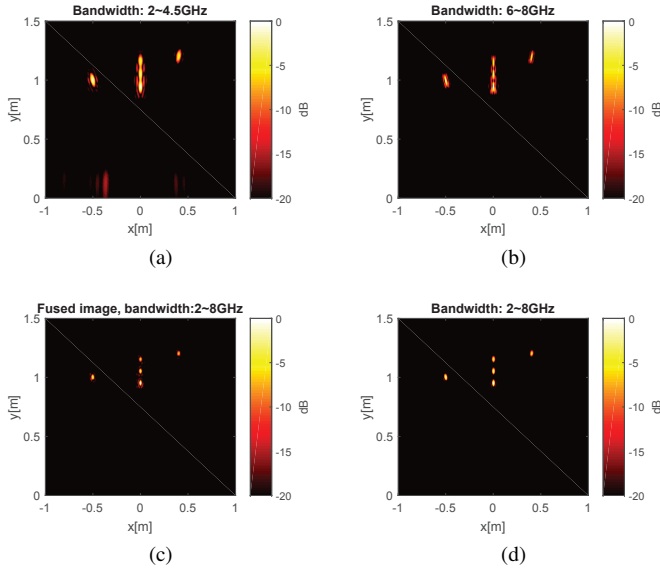
Fig. 3: Image fusion of point targets: (a) and (b) are the images of point targets with bandwidths of 2∼4.5 GHz and 6∼8 GHz, respectively. (c) is the fused image with bandwidth of 2∼8 GHz and (d) is the reference image obtained with bandwidth of 2∼8 GHz.
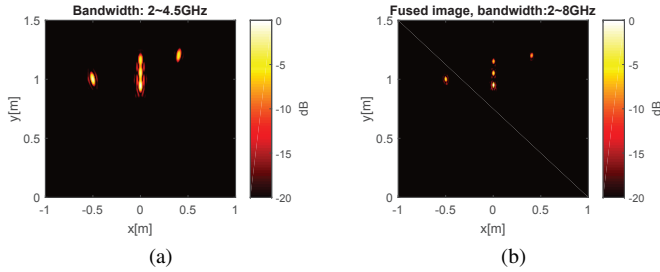

Fig. 4: Signal fusion of point targets with non-collocated antennas in low- and high-frequency subbands. (a) is the low-frequency images acquired with a down-sampled linear array and (b) the fusion image with the signals collected by down-sampled low-frequency array and the same high-frequency array as in Fig. 3.

images with the bandwidth of 2–4.5 GHz and 6–8 GHz are presented in Fig. 3(a) and (b). As the same antenna aperture was used for both low and high frequency band signals, high-frequency band signal results in finer cross-range resolution of the focused image compared to that of the low-frequency band signal. In the down-range direction, the similar resolutions are achieved for both high- and low-frequency signals as their bandwidths were equal. Fig. 3(c) shows the focused image by fusing the EM signals of the bandwidth 2–4.5 GHz and 6–8 GHz with the proposed fusion method. As an equivalent bandwidth of 2–8 GHz is achieved in the fused image, we can see that in Fig. 3(c) the two point-targets on the y-axis are more clearly resolved than those in the two subband images [Fig. 3(a) and (b)]. For comparison, the focused image with the
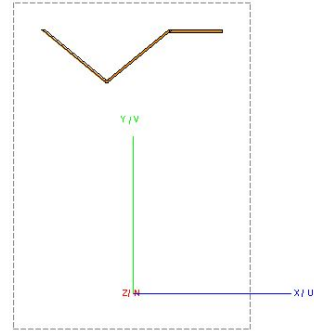

Fig. 5: Geometrical configuration for a perfect electric conductor target simulation.

EM data of the full bandwidth 2–8 GHz is shown in Fig. 3(d). One can see that the fused image is comparable to the real image reconstructed with wideband signals in terms of the spatial resolution.

To emulate the non-collocated arrays in different bands, we kept the element spacing of high-frequency array but doubled the sampling intervals (i.e., down-sampled the spatial samples by a factor of two) of the low-frequency array for a second experiment. After image formation, the EM signals collected with the down-sampled low-frequency array were focused and the image is shown in Fig. 4(a), which is comparable to Fig. 3(a). The high-subband image obtained is the same as Fig. 3(b) that we omit it for the sake of conciseness. Applying the proposed fusion approach to the signals in low- and high-frequency subbands, a fused wideband image was obtained again, as shown in Fig. 4(b). One can see that the image in Fig. 4(b) is nearly identical to that in Fig. 3(b) and the two point-targets on the y-axis are well resolved again compared to those in the two subband images.

B. Extended Target

A corner-like perfect electric conductor (PEC) object is used for extended target simulation here (see Fig. 5). The two inclined bars of the object are 16 cm in length and they form an obtuse angle of 102.7°. The length of the horizontal bar is 10 cm, and both the width and thickness of all the parts of the object are 5 mm. Similar to the point targets simulation, a linear antenna array formed by Hertz dipoles was used as the radiator. The linear antenna array was set along the x-axis with its center at the origin and the PEC object was placed on the xoy plane with a shortest distance of 0.4 m from the array, as shown in Fig. 5. The linear array was 108 cm in length. The operational bandwidths, i.e., 2–5.5 GHz and 8.5–12 GHz, were utilized as the low- and high-frequency signal bands. The intervals of antenna elements in the low- and high-frequency subbands are 1.4 and 0.7 cm, respectively. The EM synthetic data for the two operational bandwidths were generated by the EM software FEKO in the frequency domain with frequency steps of 100 MHz.

The focused images for the signals acquired with the low- and high-frequency linear arrays are shown in Fig. 6(a)–(b). Taking the fusion operation for the two subband signals in the k-space, a focused image with the enhanced resolution was
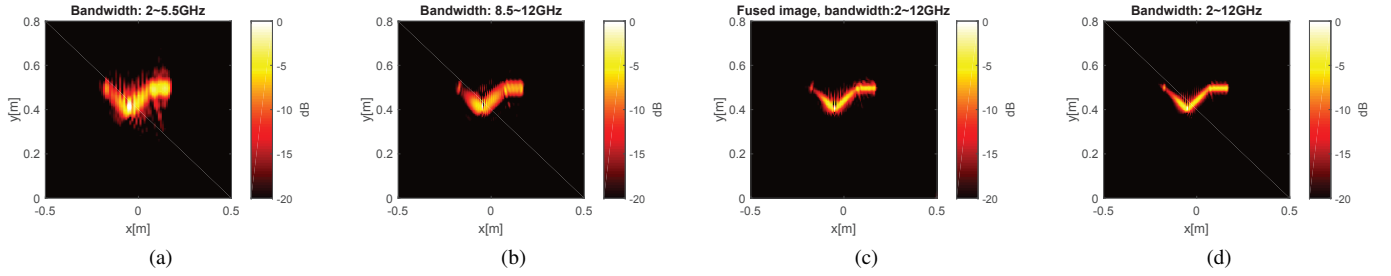
Fig. 6: Image fusion for the extended target with non-collocated arrays. (a) and (b) are the focused images of the corner-like scatterer with bandwidths of 2–5.5 GHz and 8.5–12 GHz, respectively. (c) is the fused image of the corner-like scatterer with bandwidth of 2–12 GHz and (d) is the reference image obtained with bandwidth of 2–12 GHz.
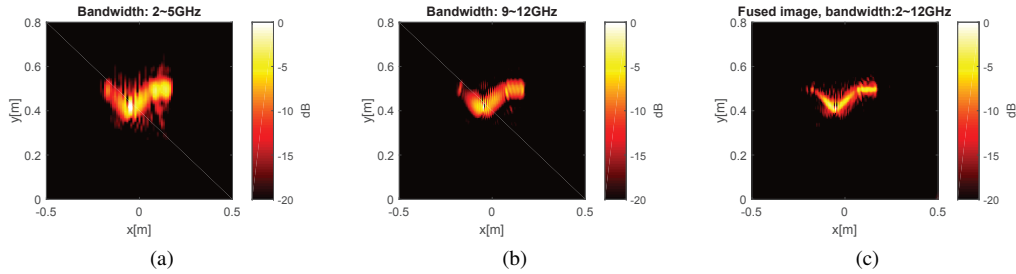

Fig. 7: Image fusion for the extended target with a 4 GHz frequency gap. (a) and (b) are the focused images with bandwidths of 2–5 GHz and 9–12 GHz, respectively. (c) is obtained by fusing the focused images with the two subbands.

Fig. 8: Image fusion for the extended target with a 5 GHz frequency gap. (a) and (b) are the focused images with bandwidths of 2–4.5 GHz and 9.5–12 GHz, respectively. (c) is obtained by fusing the focused images with the two subbands.

obtained, as shown in Fig. 6(c). For comparison, Fig. 6(d) shows the focused image with the synthetic full-band signal from 2–12 GHz. One can see that the fused image [Fig. 6(c)] is comparable to the full-band image in Fig. 6(d), especially in terms of the spatial resolutions. Therefore, the proposed k-space fusion method works effectively for the signals acquired with non-collocated antenna arrays as well in the extended target circumstance.

Finally, to demonstrate the effects of the frequency gap on the fusion results, simulations with different frequency gaps between the two operational subbands are also performed. The fusion result with two subbands of 2–5 GHz and 9–12 GHz is shown in Fig. 7(c), where the frequency gap occupies 40% of the whole bandwidth. Compared to the two subband images in Fig. 7(a) and (b), the spatial resolution of the fused image is significantly improved and more or less similar to that of the full-band image in Fig. 6(d). Moreover, a fusion simulation with a frequency gap of 5 GHz (i.e., 50% data missing), is performed and the results are presented in Fig. 8. Although a big improvement of the spatial resolution is observed in Fig. 8(c), artifacts around the focused image of the target dramatically increase and the qualities of the fused image with the proposed method degrade. Nevertheless, from Figs. 6(c), 7(c) and 8(c), one can see that the proposed fusion method enables to get well-formed images with upto 40∼50% of data missing in the whole bandwidth.

V. CONCLUSION

In this paper, we propose a matrix-pencil based approach to fuse multi-band signals in the wavenumber domain (i.e., k-

space) for high-resolution microwave imaging. The proposed approach fuses the multi-band data along each radial direction in a polar coordinate system in the k-space for 2-D imaging after some preprocessing (i.e., wavelet spectrum weighting compensation and wavefront curvature correction). Through the fusion operation, the k-space spectrum corresponding to an equivalent (ultra-)wideband signal is formed, which leads to resolution-enhanced images after focusing. Thanks to its operations in the k-space, the proposed fusion method works for the data collected by either collocated or non-collocated antennas in different frequency bands. Moreover, it also enables to get high-quality fused images with a frequency gap upto 40∼50% of the whole bandwidth. Finally, we want to mention that the proposed approach can be conveniently extended for multiband data fusion for improved 3-D imaging.

REFERENCES

[1] K. M. Cuomo, J. E. Pion, and J. T. Mayhan, "Ultrawide-band coherent processing," *Antennas and Propagation, IEEE Transactions on*, vol. 47, no. 6, pp. 1094–1107, 1999.

[2] J. E. Piou, K. M. Cuomo, and J. T. Mayhan, "A state-space technique for ultrawide-bandwidth coherent processing," tech. rep., DTIC Document, 1999.

[3] B. Tian, Z. Chen, and S. Xu, "Sparse subband fusion imaging based on parameter estimation of geometrical theory of diffraction model," *IET Radar, Sonar Navigation*, vol. 8, pp. 318–326, April 2014.

[4] Y. Q. Zou, X. Z. Gao, X. Li, and Y. X. Liu, "A matrix pencil algorithm based multiband iterative fusion imaging method," *Scientific Reports*, vol. 6, p. 19440, 2016.

[5] H. H. Zhang and R. S. Chen, "Coherent processing and superresolution technique of multi-band radar data based on fast sparse bayesian learning algorithm," *IEEE Transactions on Antennas and Propagation*, vol. 62, pp. 6217–6227, Dec 2014.

[6] Y. Zhang, T. Wang, and H. Zhao, "Multiple radar subbands fusion algorithm based on support vector regression in complex noise environment," *IEEE Transactions on Antennas and Propagation*, vol. 66, no. 1, pp. 381–392, 2018.

[7] L. D. Vann, K. M. Cuomo, J. E. Piou, and J. T. Mayhan, "Multisensor fusion processing for enhanced radar imaging," tech. rep., DTIC Document, 2000.

[8] J. Tian, J. Sun, G. Wang, Y. Wang, and W. Tan, "Multiband radar signal coherent fusion processing with IAA and apFFT," *IEEE Signal Processing Letters*, vol. 20, no. 5, pp. 463–466, 2013.

[9] P. v. Dorp, R. Ebeling, and A. G. Huizing, "High resolution radar imaging using coherent multiband processing techniques," in *2010 IEEE Radar Conference*, pp. 981–986.

[10] F. Ye, F. He, and Z. Sun, "Radar signal level fusion imaging," in *IGARSS 2008 - 2008 IEEE International Geoscience and Remote Sensing Symposium*, vol. 4, pp. IV – 1288–IV – 1291.

[11] Z. Li, S. Papson, and R. M. Narayanan, "Data-level fusion of multilook inverse synthetic aperture radar images," *IEEE Transactions on Geoscience and Remote Sensing*, vol. 46, no. 5, pp. 1394–1406, 2008.

[12] J. H. G. Ender, "The meaning of k-space for classical and advanced SAR techniques," in *International Symposium Physics in Signal and Image Processing, PSIP 2001*, (Marseille), pp. 23–38, Jan 2001.

[13] J. M. Lopez-Sanchez and J. Fortuny-Guasch, "3-D radar imaging using range migration techniques," *Antennas and Propagation, IEEE Transactions on*, vol. 48, no. 5, pp. 728–737, 2000.

[14] A. C. Kak and M. Slaney, *Principles of computerized tomographic imaging*. IEEE press, 1988.

[15] T. K. Sarkar and O. Pereira, "Using the matrix pencil method to estimate the parameters of a sum of complex exponentials," *Antennas and Propagation Magazine, IEEE*, vol. 37, no. 1, pp. 48–55, 1995.